

# Fibre-optic trapping and manipulation at the nanoscale

Yuchao Li, Hongbao Xin, Xiaohao Xu, Xiaoshuai Liu, Baojun Li\*

*Institute of Nanophotonics, Jinan University, Guangzhou 511443, China*

\*Corresponding author

DOI: 10.5185/amlett.2018.1994

www.vbripress.com/aml

## Abstract

With the initial design based on Ashkin's pioneering work in 1970, optical trapping and manipulation of micron-size particles and cells has been extensively applied in the fields of physical science and technology as well as cellular and molecular biology. However, due to the fundamental diffraction limit of light, it is difficult to extend these techniques to the nanometre range that includes nanomaterials such as nanotubes, nanowires, nanoparticles and biomolecules, which are crucial for nanoscience and nanotechnology. Recently, several approaches based on optical fibre nanoprobe have been developed and demonstrated for trapping and manipulation of nanostructures. Here, starting from basic theories of optical forces, we review the state-of-the-art in fibre-optic trapping and manipulation of different nanostructures, with an emphasis on carbon nanotubes, silver and semiconductor nanowires, upconversion and polystyrene nanoparticles, and DNA molecules. Finally, we discuss the future perspectives of nano-optical manipulation, which has considerable potential applications in a variety of scientific fields. Copyright © 2018 VBRI Press.

**Keywords:** Optical trapping, optical manipulation, nanoscale, fibre nanoprobe, diffraction limit.

## Introduction

Since the invention of optical tweezers, optical trapping and manipulation has boosted significant process in scientific areas such as biological science, materials chemistry and condensed matter physics [1-5]. Optical tweezers use optical forces exerted by focusing a free-space light with a high-numerical-aperture (NA) objective to trap and manipulate small objects, which ranges in size from a few hundred nanometres to several micrometres [6-8]. However, when applied to the nanoscale objects, the trapping strength of optical tweezers become insufficient because of the fundamental diffraction limit of light and the dramatic disturbances imposed by Brownian motion [9-11]. Moreover, the relatively bulky free-space optical systems make it lacking of flexibility and miniaturization.

Over the past few years, near-field methods were thus developed to overcome the diffraction limit and avoid the use of the bulky elements of the traditional optical tweezers. By using photonic and plasmonic devices, such as plasmonic nanoantennas [12-14], slot waveguides [15], photonic crystal resonators [16-18] and optical fibre nanoprobe (OFPs) [19-28], optical intensity can be confined into a near-field region that well below the diffraction limit, exerting sufficient trapping force to manipulate the nanoscale objects. Among these near-field techniques, OFPs have unique advantages of easy fabrication and high flexibility [29-38], which are especially suitable for three-dimensional manipulation. Using OFPs with different configurations has allowed stable trapping and flexible manipulation

of nanoscale objects, such as carbon nanotubes, silver nanowires, semiconductor nanowires, nanoparticles and DNA biomolecules. In this review, we discuss the recent progress of fibre-optic trapping and manipulation at the nanoscale and their applications.

## Optical forces on nanostructures

In this section, we first analyze how optical forces and optical torque arise at the nanoscale. For a spherical nanoparticle, which is much smaller than the incident wavelength, it can be modelled as a dipole placed in an inhomogeneous electromagnetic field [39]. This dipole is affected by a gradient force  $\mathbf{F}_{\text{grad}}$ : [40]

$$\mathbf{F}_{\text{grad}} = \frac{1}{2} |\alpha| \nabla \langle \mathbf{E}^2 \rangle \quad (1)$$

where  $\alpha$  is the polarizability of the dipole,  $\mathbf{E}$  is the electromagnetic field, the bracket denotes time averaging.  $\langle \mathbf{E}^2 \rangle$  is proportional to the electromagnetic intensity. Therefore,  $\mathbf{F}_{\text{grad}}$  points along the gradient of the optical intensity (*i.e.*, toward increasing intensity). Thus, for a light beam that strongly focused in three dimensions, a nanoparticle will be attracted toward the focal spot and trapping in an optical potential well. Here, the dipolar polarizability  $\alpha$  is a critical factor for the optical force, which determines the strength of interaction with the electromagnetic field. For a spherical nanoparticle of radius  $R$  and dielectric constant  $\epsilon$ ,  $\alpha$  can be expressed as: [41]

$$\alpha = \alpha_0 \left( 1 - \frac{ik^3 \alpha_0}{6\pi\epsilon_0} \right)^{-1}, \quad (2)$$

where  $k$  is the wavevector,  $\varepsilon_0$  is the vacuum dielectric permittivity, and  $\alpha_0$  is the quasi-static polarizability given by the Clausius-Mossotti relation: [41]

$$\alpha_0 = 4\pi\varepsilon_0 R^3 \frac{\varepsilon - 1}{\varepsilon + 2}, \quad (3)$$

Another important optical force,  $\mathbf{F}_{\text{rad}}$ , which arises from the radiation pressure on the nanoparticle when photons was scattered or absorbed by the surface of the nanoparticle, can be expressed as: [42]

$$\mathbf{F}_{\text{rad}} = \frac{\sigma}{2c} \text{Re}(\mathbf{E} \times \mathbf{H}^*), \quad (4)$$

where  $\sigma$  is the extinction cross-section of the nanoparticle,  $\mathbf{H}$  is the magnetic field, and  $c$  is the speed of light in vacuum. The direction of the resulting  $\mathbf{F}_{\text{rad}}$  points along the axis of the light beam and thus acts to disturb the trap in the axial direction. However, by strongly focusing the light in the axial direction,  $\mathbf{F}_{\text{grad}}$  can overcome  $\mathbf{F}_{\text{rad}}$ , and therefore a stable trap of nanoparticles can be achieved in three dimensions.

For above quasi-zero-dimensional nanoparticle, it is suitable to be assumed as a dipole. However, as for one and two dimensional nanomaterials, such as carbon nanotubes, nanowires, and graphene, the dipolar approximation is insufficient. In the case, the time-averaged total optical force  $\mathbf{F}$  can be calculated by integrating the optical momentum flux over a closed orientable surface  $S$  surrounding the nano-objects: [43, 44]

$$\mathbf{F} = \iint_S (\langle \mathbf{T}_M \rangle \cdot \mathbf{n}) dS, \quad (5)$$

where  $\mathbf{T}_M$  is the Maxwell stress tensor, accounting for the interaction between electromagnetic forces and mechanical momentum, which can be calculated from the optical fields:

$$\langle \mathbf{T}_M \rangle = \frac{1}{2} \text{Re} \left[ \mathbf{D} \otimes \mathbf{E}^* + \mathbf{B} \otimes \mathbf{H}^* - \frac{1}{2} (\mathbf{E}^* \cdot \mathbf{D} + \mathbf{H}^* \cdot \mathbf{B}) \mathbf{I} \right], \quad (6)$$

where  $\mathbf{D}$  is the electric displacement,  $\mathbf{B}$  is the magnetic flux field, and  $\mathbf{I}$  is the isotropic tensor. The time-averaged optical torque  $\mathbf{T}$  on the trapped nano-objects then can be calculated in an analogous way as: [45]

$$\mathbf{T} = \int \mathbf{r}_p \times d\mathbf{F}_p, \quad (7)$$

where  $d\mathbf{F}_p$  is the optical force element at the interaction point  $p$  (the arbitrary interaction point on the nano-objects), and  $\mathbf{r}_p$  is the position vector pointing from the central point of the nano-objects to the interaction point  $p$ . This optical torque can be used to rotate the trapped nanostructures and control their orientation, which is critically important for the nanostructure assembly.

### Carbon nanotubes

Carbon nanotubes (CNTs) are currently considered as promising building blocks for a wide variety of applications, because of their unique optical and

electronic properties that arise from their quasi-one-dimensional character [46-48]. Despite the increasing researches conducted in recent years, the integration of CNTs in practical applications is difficult because of a lack of efficient manipulation methods for single CNTs. In particular, one of the greatest challenges for the integration of individual CNTs is the arrangement of CNTs with controllable orientation and position [49-51]. This difficulty imposed by the dramatic Brownian motion and the large rotational diffusion coefficient of the CNTs in a solution [52]. Although optical tweezers have been successfully used to trap bundles of single or multi-wall CNTs and aggregate massive CNTs, it is insufficient to manipulate a single CNT, especially to optically trap a CNT and simultaneously orient it [53, 54]. In this section, we will show a nano-optical method for the controlled manipulation and orientation of a single CNTs using an OFP [23].

**Fig. 1** schematically shows the manipulation and orientation of a single CNT by launching a 980-nm wavelength laser beam into an OFP, which has a nanotip of 200-nm diameter and was fabricated by heating and drawing a single-mode optical fibre [23]. The strongly focused beam outputted from the OFP can exert an optical gradient force on a CNT that was trapped near the end of the OFP. Then the trapped CNT was oriented and shifted along the OFP axis by the radiation pressure force, which raised from the strong optical scattering and absorption of the CNT. In the practical experiment, individual CNTs cannot be observed under a conventional optical microscope because of their nanometre size. To directly observe the manipulation process of a single CNT, a blue laser beam is directed into a tapered optical fibre that was oppositely placed to the OFP and with its end was also immersed in the suspension.

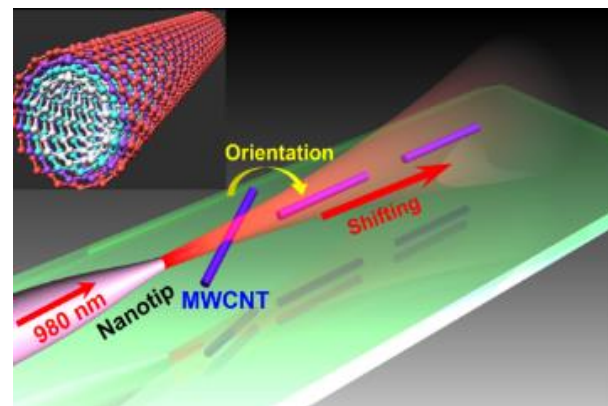


**Fig. 1.** Optical trapping, orientation and shifting of a single carbon nanotube by using a 980-nm light beam that was launched into the OFP. The inset shows a representative structure of the carbon nanotube.

It is worth mentioning that the input optical power of the blue laser beam was only 35  $\mu\text{W}$ . So that the optical force that is exerted on each CNT by such a low optical power was too weak to affect the manipulation of the CNT and thus had no influence on the CNTs. After irradiating by the blue laser beam, the CNTs

could be directly observed by the optical scattering of the blue light from the surfaces of the CNTs, which was contributed to the large Rayleigh scattering cross-sections of the CNTs. Before trapping, the CNTs randomly moved in the suspension because of the Brownian motion. Then the 980-nm trapping laser beam was launched into the OFP at different optical powers. In this case, the motion of the CNTs was dominated by the competition among the optical forces, the viscous drag, and the Brownian motion. The results showed that when optical power was larger than 40 mW, a CNT was trapped at the tip of the OFP by the optical gradient force exerted on the CNT, and then was rotated along the optical axis by the optical torque. During this orientation process, the trapped CNT moved along the OFP axis because of the optical scattering force [23].

**Fig. 2a** showing a bright-field optical image of the OFP that was illuminated by a blue light when it was immersed in a CNT suspension, while **Fig. 2b** schematically shows the orientation angle and shift distance of the trapped CNT along the optical axis. To illustrate the optical orientation and manipulation process, **Fig. 2c** shows a time sequence of the experimental result for a single CNT with a length of 0.9  $\mu\text{m}$  and diameter of 50 nm. At the beginning, a single CNT was trapped near the OFP with a certain angle and distance (**Fig. 2c1**). Then, the trapped CNT is oriented at different angle and has shifted to various distance controlled with the optical scattering force (**Fig. 2c1-9**). After the CNT moved far away from the OFP, the exerted optical force become weaker, and in this case, the motion of the CNT was dominated by the Brownian motion again (**Fig. 2c10**) [23].

This proposed method has demonstrated that the OFP can be applied for the controlled orientation and targeted manipulation of a single CNT. The optical force generated by the outputted light beam near the OFP can overcome the strong Brownian motion. This capability to controllably rotate and manipulate a single CNT provides a potential possibility for assembly of one-dimensional materials into desired arrangements and will facilitate the development of high-precision integration of CNT structures [23].

### Silver nanowires

Silver (Ag) nanowires are served as a significantly promising element for nanophotonic circuits because of their intrinsic physical properties induced by surface plasmonic resonances that enable nanoscale confinement of light [55-57]. In order to integrate Ag nanowires into nanophotonic devices, it will be crucial to manipulate and orient them with high angular precision [58]. However, direct optical orientation of single Ag nanowire, especially in an aquatic environment, is difficult because the Ag nanowire will be influenced by the intense Brownian motion and strong viscous drag [59]. Optical forces has been verified that can provide a promising approach to orient

and manipulate nanoscale objects. Recently, an OFP-based method for a controllable orientation of a single Ag nanowire was successfully demonstrated by optical torque, which was generated by radiation pressures that arises from the optical fields outputted from the two OFPs and directly exerted on the Ag nanowire [20].

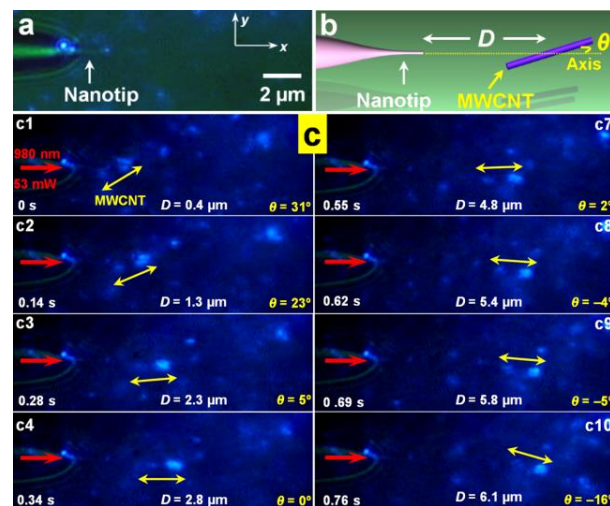


**Fig. 2.** Optical trapping, orientation and shifting of single carbon nanotube with an OFP. (a) Optical image of an OFP with launching a 473-nm light beam. (b) Schematic of optical trapping and orientation of a single carbon nanotube. (c) Dark-field images showing the trapping, orientation and shifting of a single carbon nanotube along the OFP axis [23].

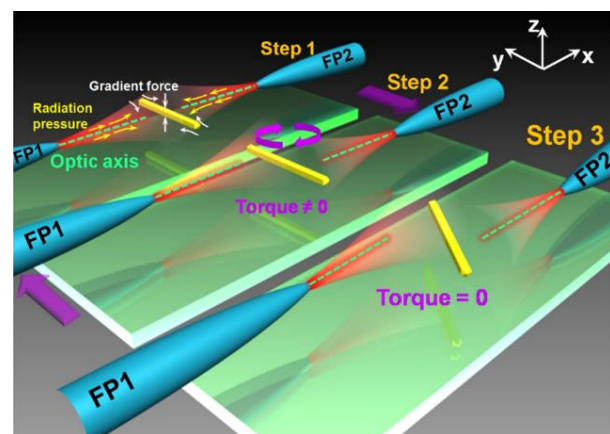


**Fig. 3.** Schematic of optical orientation process for a single silver nanowire with two opposite OFP. Step 1 showing a silver nanowire is stably trapped using two counter-propagating light beams. When the two OFPs are moved in an opposing direction, the nanowire is controllably rotated by the optical torque (Step 2). After stopping the movement, the nanowire is stationary and so that has a new orientation (Step 3) [20].

**Fig. 3** schematically shows the experimental process to illuminate the orientation mechanism of the OFPs. To trap and rotate a single nanowire with two OFPs, a 980-nm laser beam was coupled into both fibre 1 (OFP1) and fibre 2 (OFP2) through a 1x2 coupler (splitting ratio: 1:1). These two OFPs were fixed on tunable microstages that can move the OFPs in opposite directions with a manipulation resolution of 50 nm. The tips of the OFPs were inserted in the nanowire suspension. The Ag nanowire manipulation and rotation

process can be described as follows: first, OFPs 1 and 2 were moved to approach an Ag nanowire and the 980-nm trapping laser beam was directed into the OFPs to trap the nanowire by these two counter-propagating laser beams. Then, these two OFPs were manipulated in opposite directions along the  $y$  axis to rotate the trapped nanowire *via* optical torque, which is induced by asymmetric distributions of the radiation pressures from the OFPs. After stopping the movement of the OFPs, the rotation of the nanowire was also stopped, with the resulting orientation controlled by the offset between the two competing radiation pressures. Therefore, the orientation of the trapped Ag nanowire can be controlled by changing the distance between two OFPs in the vertical direction [20].

**Fig. 4** shows time-consecutive experimental images of the orientation of a single Ag nanowire (length: 6.5  $\mu\text{m}$ , diameter: 600 nm) that was induced by verifying the distance between the two OFPs in the  $y$  direction. The panels on the right indicates the corresponding angular orientation of the nanowire. The lateral distance between the two OFPs was fixed as 23  $\mu\text{m}$ . **Fig. 4a** shows that at the beginning of the process, the Ag nanowire was stably trapped by radiation pressure with an angle of  $82^\circ$ . By simultaneously moving OFP 1 in the  $+y$  direction and OFP 2 in the  $-y$  direction, the trapped nanowire was rotated clockwise by the optical torque. **Fig. 4a–e** showing the angular orientation of the nanowire was continuously changed from  $82^\circ$  to  $-70^\circ$ , that is, the nanowire was rotated by  $152^\circ$ . It's worth noting that the trapped nanowire can also be rotated in the counterclockwise direction by the inverse movement of the OFPs because this system was symmetric. In the experiments, when the vertical distance between the two OFPs was larger than 6.0  $\mu\text{m}$ , the optical torque become too weak to rotate the nanowire. Fortunately, this limitation can be overcome by increasing the input optical power or reducing the lateral distance between the OFPs [20].

In addition to controlling the orientation of a single Ag nanowire, the continuous rotation of a single Ag nanowire was also demonstrated by using two OFPs. **Fig. 5** schematically illuminates the continuous rotation of an Ag nanowire, with its end was bound to the glass slide with the electrostatic attraction. Different from the configuration of the orientation of the Ag nanowire as mentioned above, here, the two counter-propagating beams were coherent because the length difference between the two OFPs was smaller than coherent length of the input wavelength. In this case, an optical vortex can be generated by the interference of these two non-coaxial coherent beams. For an example, the inset of **Fig. 5** indicates the simulated  $|E/E_0|^2$  distribution and the Poynting vector for the output light near the OFPs. The result shows that the Poynting vectors are vortex-shape in bright regions and the centre of the optical vortices are aligned along a direction of  $19^\circ$  relative to the  $+x$  direction. When the Ag nanowire is located in this optical vortex, the interaction between the nanowire

and vortex can exert a strong optical torque on the nanowire that will cause a continuous rotation. The rotation speed can be controlled by the input optical power. This ability to persistently rotate a single nanowire can find various applications, such as light-driven nano-motors [21].

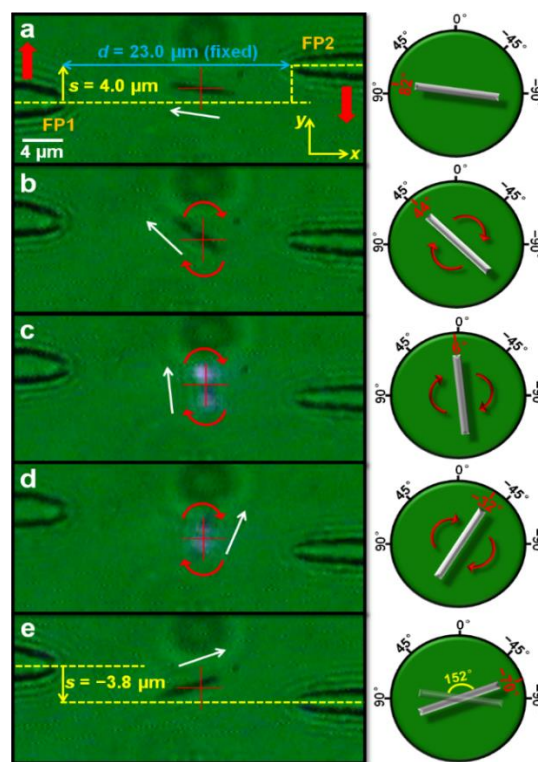


**Fig. 4.** Optical rotation and orientation process for a single silver nanowire using two OFPs with wavelengths of 980 nm and input optical powers of 20 mW in each fibre. (a–e) Optical images showing optical rotation and rotation of the single silver nanowire in response to a decreasing distance between fibres 1 and 2 in the  $y$  direction. The crossed red symbol denotes the reference position, the white arrow indicates the orientation of the nanowire, and the dashed yellow line shows the axis of each fibre. The panels on the right showing the angular orientations of the trapped nanowire corresponds to (a)–(e) [20].

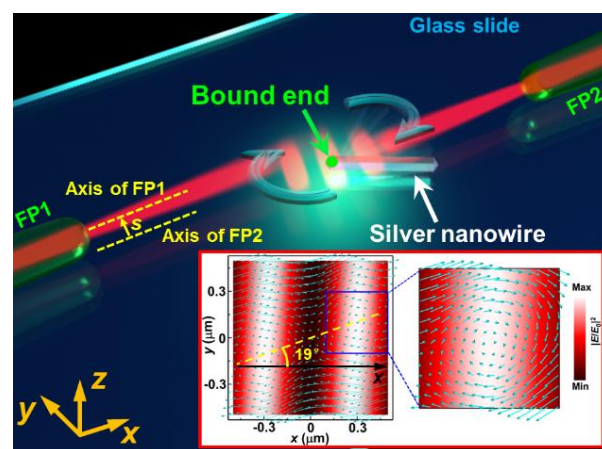


**Fig. 5.** Schematic showing a continuous rotation of a single silver nanowire. The inset shows the simulated  $|E/E_0|^2$  distribution. An optical vortex is generated by using two non-coaxial coherent beams from two OFPs with an axial distance  $d = 32.8 \mu\text{m}$  and a transverse distance  $s = 1.0 \mu\text{m}$  [21].

## Semiconductor nanowires

Semiconductor nanowires have attracted considerable attention because their potential use as building blocks for many miniaturized optical and electrical devices [60, 61]. Among various semiconductor nanowires, zinc oxide (ZnO) nanowires are one of the most promising nanomaterials owing to their unique physical properties, such as wide band gap and piezoelectric features [62, 63]. To function ZnO nanowires as practical building blocks, techniques for assembling and manipulating single ZnO nanowires are critically important. Benefiting from high spatial accuracy and controllable optical parameters, optical tweezers have become an appealing approach to manipulate ZnO nanowires with high resolution [64]. However, optical tweezers are limited by relatively bulky elements of high-NA objective and free-space lens system, which lead to the lack of flexibility and miniaturization, especially for the applications in integrated optics. OFPs have high flexibility and miniaturization, which can be functioned as a compact and powerful technique for trapping and manipulation of single ZnO nanowires [28].

**Fig. 6** shows the experimental results of the trapping and manipulation of a single ZnO nanowire. To exert an effective optical force on the nanowire, a 980-nm laser beam with an optical power of 52 mW was launched into the OFP. When the OFP moved precisely using the fibre microstage (movement precision: 50 nm), the trapped nanowire will be manipulated by the optical gradient force. Therefore, two-dimensional manipulation of the nanowire can be realized by simply controlling the OFP (**Fig. 6a–f**). Specifically, **Figs 6a and b** show that the OFP was moved with a distance of 10.3  $\mu\text{m}$  in 2.16 s in the  $-x$  direction. The trapped nanowire also manipulated along with the movement of the OFP at an average velocity of  $-4.8 \mu\text{m/s}$ . Then, the nanowire was manipulated in the  $+x$  direction by moving the OFP (**Figs. 6c and d**). After that, the trapped nanowire was also made to move in the  $y$  direction (**Fig. 6e and f**). This result reveals that the precise manipulation of a single nanowire can be realized by moving the OFP steadily and flexibly [28].

After trapping a single ZnO nanowire, the extended focal spot from the OFP can generate strong gradient force on other nanowires, resulting in aligning more nanowires sequentially along the optical axis of the OFP. Therefore, by manipulating the first trapped nanowire to approach to other suspended nanowires, the suspended nanowires can also be trapped and aligned near to the former nanowire (**Fig. 7**). The experimental process as followed: at the beginning, the first nanowire was trapped at the tip of the OFP with an optical power of 29 mW (**Fig. 7a**). Then, the first nanowire was precisely moved to approach the second nanowire, which was rotated to the optical axis because of the torque induced by the optical force, and trapped at the rear end of the first nanowire (**Fig. 7b**). Subsequently, the optical power was increased to 45 mW to enhance

the optical forces and five nanowires were assembled and aligned along the optical axis as a nanowire chain (**Figs. 7c and d**). It should be noted that the formed nanowire chain will finally move away from the OFP, because the optical scattering force became dominate when nanowires were far from the focal spot. To stably maintain the nanowire chain, an oppositely placed fibre can be applied to balance the optical scattering force. Overall, the manipulation of ZnO nanowires with an OFP could find potential applications in assembling semiconductor nanophotonic structures [28].

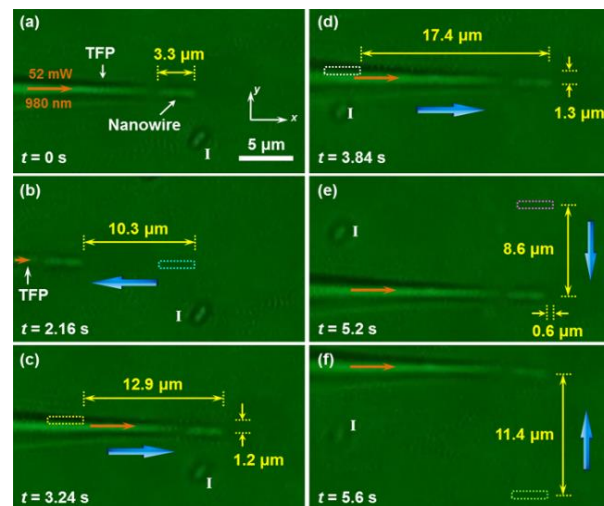


**Fig. 6.** Optical microscope images show the two-dimensional manipulation of a single ZnO nanowire. The input optical power of the 980-nm laser beam was set at 52 mW. (a) At  $t = 0$  s, a single nanowire was stably trapped at the tip of the OFP. Nanowire I, as a reference point, was adhered to the glass slide *via* van der Waals force. (b–d) Optical manipulation of the trapped nanowire in the  $x$  direction. The blue arrow denotes the direction of the manipulation. The blue dashed rectangle shows the nanowire position as it was in panel (a), the yellow dashed rectangle indicates the nanowire position as it was in panel (b), and the white dashed rectangle denotes the nanowire position as it was in panel (c). (e, f) Optical manipulation of the trapped nanowire in the  $y$  direction. The pink dashed rectangle shows the nanowire position as it was in panel (d), and the green dashed rectangle denotes the nanowire position as it was in panel (e) [28].

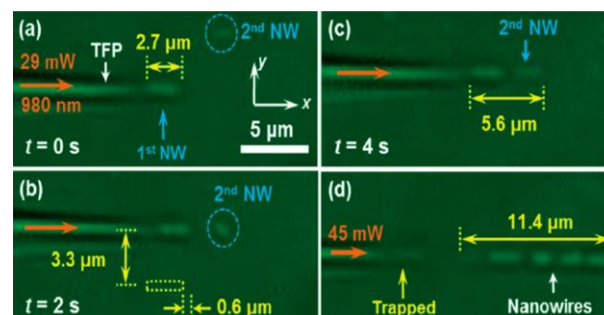


**Fig. 7.** (a–c) Optical microscope images show optical assembly of multiple ZnO nanowires. (a) At  $t = 0$  s, the first nanowire was trapped at the tip of the OFP and then a second nanowire was randomly suspended in water. (b) At  $t = 2$  s, the first nanowire moved with a distance of 3.3  $\mu\text{m}$  in  $y$  direction and 0.6  $\mu\text{m}$  in  $x$  direction to approach the second nanowire. The yellow dashed rectangle indicates the nanowire position in panel (a). (c) At  $t = 4$  s, the second nanowire was trapped at the rear end of the second nanowire. (d) Optical assembly of five nanowires into a chain with a total length of 11.4  $\mu\text{m}$  [28].

## Upconversion nanoparticles

Upconversion fluorescent nanoparticles (UCNPs), which convert near-infrared excitation to ultraviolet or visible luminescence, have been served as a promising candidate for the traditional fluorescent nanomaterials owing to their unique physical and chemical features, such as minimized spectral cross-talk, negligible photodamage, large penetration depth and less autofluorescence noise [65-68]. Although UCNPs have been extensively applied for biological imaging of mammalian cells such as cancer cells, it is difficult to image bacteria not only because bacteria generally have subwavelength sizes, but also the fluorescence efficiency of UCNPs is smaller than 1%. [69-71]. Furthermore, in practical applications, the bacteria frequently swim with flagella or flow with biofluids, which will further weaken the detected upconversion fluorescence owing to relatively short integration time of charge-coupled device camera or semiconductor photodetector. Additionally, the traditional fluorescence-based methods are applied for imaging a mess of bacteria. Imaging and detection of bacteria with single-cell resolution, which requires much higher sensitivity, are more important to identify the bacterial heterogeneity and investigate their cell-cell interactions [72, 73]. More recently, an optical co-trapping strategy has been proposed and successfully demonstrated to achieve the single-cell imaging and real-time detection of small bacteria by simultaneously trapping the targeted bacteria and UCNPs using a single OFP [26, 27].

**Fig. 8a** schematically depicts the optical trapping of an *E. coli* cell labeled with UCNPs. First, a single UCNP undergoing strong Brownian motion was trapped at the tip of the OFP with a 980-nm light beam launched into the fibre. The un-trapped UCNPs were unable to directly observe due to the nanometer size of the UCNPs. After being stably trapped, the UCNPs can be clearly observed with the green fluorescence emitted by the excitation of the 980-nm near-infrared light beam. The 980-nm light beam reflected by the trapped UCNP transmitted along the OFP and then monitored in real time through a photodetector. By manipulating a trapped UCNP to approach a targeted *E. coli* cell by the OFP, the cell was then trapped together and connected to the firstly trapped UCNP by the optical gradient force. After trapping the *E. coli* cell, another adjacent UCNP was also trapped and connected to the end of the *E. coli* cell. As a result, two UCNPs were trapped on the both ends of a single *E. coli* cell. Under the near-infrared excitation, these two UCNPs emitted green fluorescence that are visible in the dark field. Therefore, a single cell is specifically labeled. It should be noted that the 980-nm light beam was applied for both the excitation and trapping light source, and thus the trapping, detection and labeling can be performed by using only a single OFP and a light source, which can greatly simplify the optical experimental setup [26].

As an example of single-bacteria analysis, this approach can be applied for single-bacterium sizing. **Fig. 8bI-IV** shows the bright-field optical images of labeled single bacteria of different lengths with the UCNPs, and **Fig. 8cI-IV** shows the corresponding dark-field images. With an input optical power of 22 mW, the UCNPs and bacteria were stably trapped without observable vibration in the suspension. The sizes of the labeled single bacteria can be accurately measured from the reflected real-time signals. When a single labeled bacterium being trapped, an increase in the reflection signal was obtained for compared with the OFP without trapping. There is a one-to-one correspondence between the signal incensement and the sizes of the trapped bacteria. Therefore, the reflection signal can be used for high-resolution single-bacterium sizing. The ability of trapping and detection of UCNPs and bacteria can be used for precise single-bacterium labeling and analysis, with great potential for specific labeling and real-time analysis of pathogenic bacteria [26].

Besides the signal detection of the bacteria, high-resolution and real-time image of pathogenic bacteria can be achieved by coupling the UCNPs to the surface of the pathogenic bacteria and then using a bio-microlens to stably trap the targeted bacteria and enhance the upconversion fluorescence of UCNPs. In this technique, a living yeast cell or human cell was employed to function as a natural bio-microlens. This living bio-microlens, which was stably bound to the tip of an OFP, could focus the excitation light into a subwavelength region so that the upconversion fluorescence of UCNPs (the used UCNPs were core-shell NaYF<sub>4</sub>:Yb<sup>3+</sup>/Tm<sup>3+</sup> nanoparticles) was enhanced by two orders of magnitude. Benefiting from the strong fluorescence enhancement, single-cell imaging and real-time detection of labeled pathogenic bacteria have been achieved in the dark fields. Two species of bacteria, *i.e.* *Escherichia coli* and *Staphylococcus aureus*, which are responsible for half of all bacterial infectious diseases, were used as biosamples. The bacteria were labeled with UCNPs by mixing the UCNPs and bacteria in the liquid environment. Then they were coupled together through electrostatic attraction effect because the surface of the bacteria is negatively-charged, while the UCNPs is positively-charged by the amine-functionalization (**Fig. 9a**).

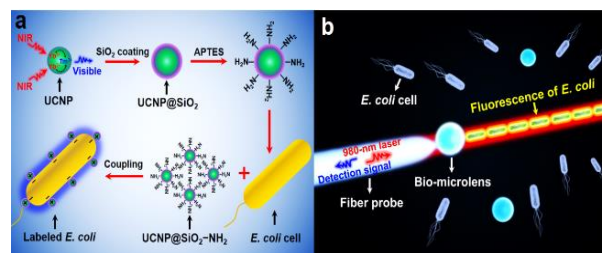


**Fig. 9.** (a) Schematic shows the preparation process for labelling the *E. coli* cells with the core-shell amine-functionalized UCNPs (UCNP@SiO<sub>2</sub>-NH<sub>2</sub>). The bacteria and UCNPs are stably coupled together via electrostatic attraction. (b) Schematic illustration of the manipulation and detection of an *E. coli* chain with a bio-microlens at the tip of an OFP [27].

It should be noted that this bacterial labelling method can avoid biochemical treatments of antibodies and their coupling was strong enough to remove the excess UCNP with a high-speed centrifugation without obvious influence of the labeled UCNP. As shown in **Fig. 9b**, a schematic illustrates the fluorescence imaging and detection of the bacteria by an OFP bound with a bio-microlens. By directing a 980-nm light beam with an optical power of 3 mW into the OFP, the bio-microlens was optically trapped at the tip of the fibre and then the light beam was concentrated into a subwavelength focal spot. Mentioned that the light beam with 980-nm wavelength is weakly absorbed by biological matter and highly efficient for exciting the upconversion fluorescence from the UCNP. By moving the OFP in three dimensions, the bacteria labeled with UCNP were trapped in the highly focused light spot outputted from the bio-microlens. After trapping a single bacterium, the 980-nm laser beam was confined and propagated along the bacterium, and then more bacteria can be trapped and connected orderly by the optical gradient force and finally results in a bacteria chain. The refractive index contrast of the bacteria chain was calculated as about 4.2%, which is higher than 3.6% of standard core-cladding single-mode optical fibres (SMF-28), indicating that the bacteria chain can act as a biological waveguide. Therefore, the formed bacteria chain can transmit the 980-nm excitation light beam that can efficiently excite the fluorescence from the bacteria, which was directly observed under the optical microscope in a dark-field mode. During the trapping and imaging process, the fluorescent and backscattering signals of the bacteria can propagate back along the bio-microlens and was then detected with the OFP in real time. **Figs. 10a** and **10b** show the fluorescent images of *E. coli* and *S. aureus* chains, respectively, which were optically assembled by the bare OFP (**Figs. 10a1** and **b1**) and bio-microlens (**Figs. 10a2** and **b2**). It can be seen that, the upconversion fluorescence intensity of the bacteria chains assembled by the bio-microlens was obviously enhanced. The measurement result shows that the maximum fluorescent intensity of the bacteria was enhanced by 110 times with the bio-microlens. This enhancement of the fluorescence was derived from two contributions: first, the strongly focused capability of the bio-microlens that can enhance the excitation ratio of the fluorescence; second, the microlens has a high NA (0.95) that improves the collection efficiency of the fluorescence signal. This technique uses natural biomaterials to form the living natural microlenses, which are highly biocompatible and free of nano-manufacturing processes. With the features of biocompatibility, miniaturization and sensitivity, the approach could find applications in bioimaging, nanosensors and single-cell analysis [27].

### Polystyrene nanoparticles and biomolecules

In this section, we will discuss the three-dimensional nano-optical manipulation of single polystyrene (PS)

nanoparticles and DNA biomolecules with photonic nanojets [24, 25]. The photonic nanojets, which are sub-diffraction limited light beams on the shadowed-side of a spherical dielectric microlens, resulted from the constructive interference of the optical field [74-76]. After firstly proposed by Chen *et al*, photonic nanojets have been widely applied in physical and biological fields [77-79]. Some previous works have demonstrated that the backscattering, fluorescent and Raman scattering signals from nanoparticles can be significantly enhanced by the photonic nanojets [80, 81]. The optical confinement and signal enhancement performances of photonic nanojets provide a new exciting possibility for three-dimensional trapping and manipulation of single sub-100-nm nanoparticles or biomolecules [24, 25].

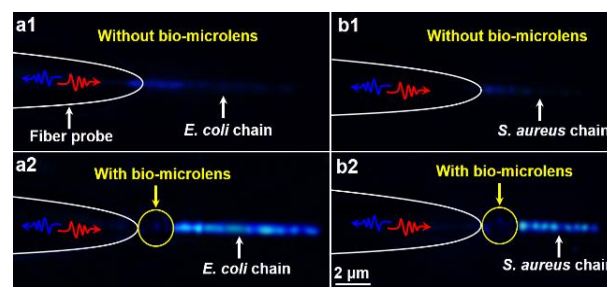


**Fig. 10.** Optical manipulation and detection of *E. coli* and *S. aureus* chain. (a) Fluorescent images showing an *E. coli* chain with six bacteria was assembled by an OFP (a1) without a bio-microlens and (a2) with a bio-microlens. The red and blue arrows denote the input light and detection signal, respectively. (b) Fluorescent images showing a *S. aureus* chain with eight bacteria was optically assembled by an OFP (b1) without a bio-microlens and (b2) with a bio-microlens [27].

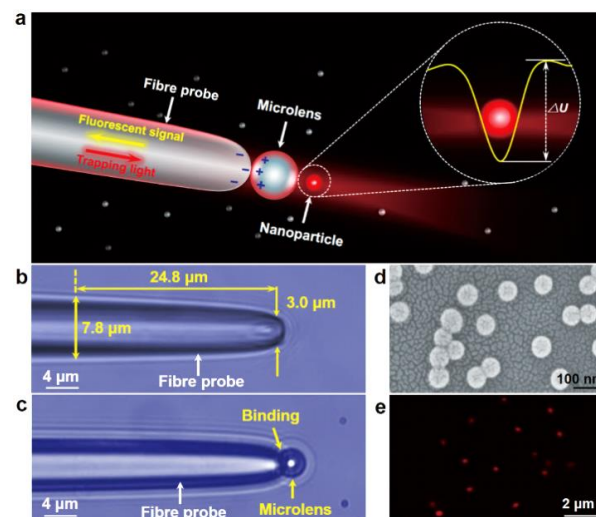


**Fig. 11.** Experimental schematic and material characterization. (a) Schematic illustrating the manipulation and detection of a single nanoparticle using a photonic nanojet. The inset shows a nanoparticle trapped in a potential well that was formed by the photonic nanojet. The maximum potential difference is denoted as  $\Delta U$ . (b) Optical microscope image of the OFP that was used in the experiments. (c) Optical microscope image of the OFP when stably bound to a 3  $\mu\text{m}$  microlens by electrostatic attraction. (d) SEM image of fluorescent PS nanoparticles with diameters of  $85 \pm 2$  nm. (e) Fluorescent image of the fluorescent PS nanoparticles showing the 639 nm emission that was excited in the solution using a 398 nm laser [24].

To generate a photonic nanojet, a titanium dioxide (TiO<sub>2</sub>) microlens was bound to the tip of an OFP with electrostatic attraction in aquatic environment (Figure 11a). The photonic nanojet, which was focused behind the microlens, can form a three-dimensional nano-optical potential well that stably trapped a single nanoparticle in a non-contact and non-invasive manner, as schematically shown in the inset of Fig. 11a. To hold the microlens and pre-focus the light, an OFP was fabricated by heating and drawing a single-mode optical fibre (Figure 11b). By modifying the charges on the surfaces of the OFP and the microlens, the nanoprobe-microlens structure was stably bound and maintained (Fig. 11c). To experimentally verify the manipulation and detection ability of the photonic nanojet, the fluorescent PS nanoparticles (average diameter: 85 nm), which can be considered as rough approximate models for viruses and small spherical bacteria were firstly used as targets (Fig. 11d). Under excitation of a 398-nm ultraviolet laser, the emission red fluorescence of PS nanoparticles (emission peak: 639 nm) can be directly observed with the optical microscope (Fig. 11e) [24].

To trap nanoparticles, the OFP was mounted on a fibre positioner (resolution: 50 nm), and the tip of the OFP was inserted into a microfluidic channel that contained a mixture of microlenses and fluorescent PS nanoparticles. The tail end of the OFP was connected to the stem of a Y-branch fibre coupler. The two arms of the coupler were connected to a trapping laser source and a photodetector with a bandpass filter. An ultraviolet light beam, which was launched into another fibre, was used to excite the fluorescence of the nanoparticles. To monitor the binding process of the microlens, the reflected signal ( $R_1$ ) was obtained in real-time (Fig. 12a). A stable binding event was indicated by an abruptly increased  $R_1$ . The nanoprobe-microlens structure (Fig. 12a1 and a2) can be freely controlled in three dimensions for subsequent experiments. After the trapping laser beam was sent into the fibre, a single 85 nm fluorescent PS nanoparticle was stably trapped into the photonic nanojet by the strong optical gradient force, and a real-time reflected signal  $R_2$  was also obtained to detect the trapping event (Fig. 12b). The output optical power from the microlens was measured as 3.2 mW and thus the local intensity in the trap was estimated as  $1.2 \times 10^{10}$  W m<sup>-2</sup>, which is lower than that of the conventional optical tweezers (which typically ranges from  $1 \times 10^{11}$  to  $1 \times 10^{12}$  W m<sup>-2</sup>). The signal  $R_2$  shows three consecutive regimes: before trapping, stable trapping and release of the single nanoparticle. The insets of Fig. 12b indicate corresponding optical images of this trapping process. When the nanoparticle dropped into the trap, the intensity of  $R_2$  abruptly increased owing to the backscattering signal from the trapped nanoparticle. In addition, the fluctuation of  $R_2$  become larger because of Brownian motion of the nanoparticle. To quantify the trapping stiffness ( $\kappa_{trap}$ ) of the photonic nanojet, a typical frequency-domain analysis (Fig. 12c), which is

considered as one of the most accurate method to calculate optical forces, was performed [82, 83]. First, a histogram was obtained for  $R_2$  counts from the trapping event (the inset of Fig. 12c).

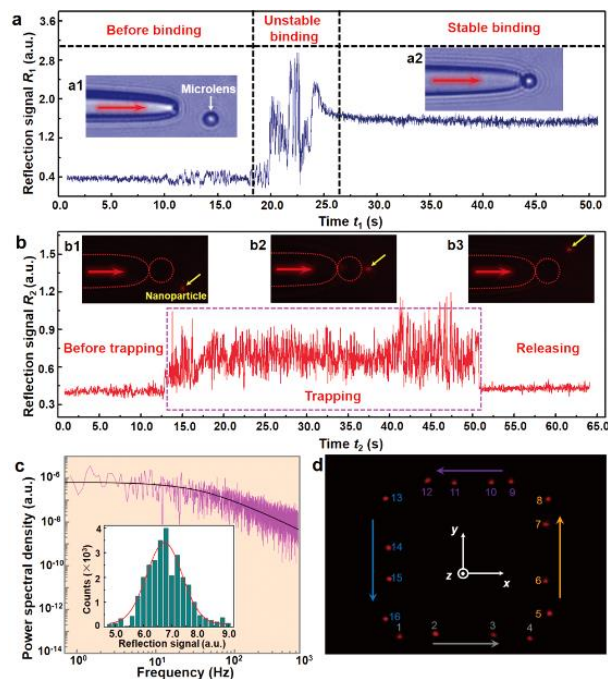


**Fig. 12.** Three-dimensional manipulation of single nanoparticle. (a) Real-time trace of the reflected signal of the microlens binding process. The signal was detected by the OFP, which was connected to a photodetector. The insets show optical images taken (a1) without and (a2) with a microlens bound to the tip of the OFP. (b) Real-time trace of the reflected signal of an 85 nm fluorescent PS nanoparticle in the trapping process. The insets show fluorescent images taken (b1) before trapping, (b2) during trapping, and (b3) on release. (c) Power spectral density of the trapping process and curve fitted (black) to the Lorentzian model with corner frequency  $f_c = 89.5$  Hz. The inset shows a histogram and the curve (red) fitted to a Gaussian model, which indicates that the nanoparticle was trapped within a harmonic potential. (d) Composite fluorescent image that shows manipulation of the trapped nanoparticle in the  $x$ - $y$  plane by controllable movement of the OFP [24].

The histogram can be fitted with the Gaussian distribution, which reveals that the nanoparticle was trapped by a harmonic optical potential well and exerted a harmonic optical force. This optical force can be expressed as  $F = -\kappa_{trap} x$ , where  $x$  is the nanoparticle distance relative to the center of the trap. As shown in Fig. 12c, the power spectrum of the nanoparticle fluctuations can be fitted by a Lorentzian function with a centre frequency of  $f_c = 89.5$  Hz. As a result, the  $\kappa_{trap} = 2\pi\beta f_c$  was calculated as  $0.13$  pN nm<sup>-1</sup> W<sup>-1</sup>, where  $\beta = 6\pi\eta r$  is the Stokes drag on the nanoparticle,  $\eta$  is the viscosity of the medium at room temperature and  $r$  the radius of the nanoparticle. For comparison with other methods, all the  $\kappa_{trap}$  values were scaled for an 85 nm particle, because the optical force is proportional to the third power of the particle radius [84]. The measured  $\kappa_{trap}$  of the photonic nanojet was comparable to that of slot waveguides (scaled  $\kappa_{trap}$  of  $0.12$  pN nm<sup>-1</sup> W<sup>-1</sup>) [15] and two orders of magnitude higher than that of the conventional optical tweezers (scaled  $\kappa_{trap}$  of  $0.0007$  pN

$\text{nm}^{-1} \text{W}^{-1}$ ) [5] or plasmonic tweezers (scaled  $\kappa_{\text{trap}}$  of  $0.001 \text{ pN nm}^{-1} \text{W}^{-1}$ ) [85]. After stably trapping, controllable manipulation of the single nanoparticle can be performed in three dimensions by moving the OFP. As shown in Figure 12d, the movement trajectory of the nanoparticle was plotted by superimposing optical images that were captured at different instants separated by the same time interval. The nanoparticle was manipulated over total distances of about  $60 \mu\text{m}$  in the  $x$ - $y$  plane and about  $10 \mu\text{m}$  in the  $z$  direction. The ability to move a single sub-100-nm particle to a desired position in three dimensions could find potential applications in nanomaterials science for nanoparticle patterning and the highly-regulated nanostructure assembly [24].

Compared with the dielectric nanoparticles, single biomolecules are more difficult to manipulate because of their irregular shape, extremely small size and low refractive index. Fortunately, optical three-dimensional manipulation of a single biomolecule can be also performed by the photonic nanojet. For example, plasmid DNA molecules (3.4 kilobases long) were used as targeted biomolecules. Before the trapping, the DNA molecules exhibited dramatic Brownian motion in the suspension. After the trapping laser beam with an optical power of  $5 \text{ mW}$  ( $1.9 \times 10^{10} \text{ W m}^{-2}$ ) was directed into the OFP, a single DNA molecule was stably trapped and then manipulated in three dimensions (Fig. 13a–c). In this trapping experiment, the DNA molecules were illuminated in the transverse side by launching a blue light with an optical power of  $150 \mu\text{W}$  into the suspension. After the irradiation, the scattering light from single DNA molecules can be directly observed in the dark field (Fig. 13d). The trapped DNA will be finally released owing to the increased Brownian motion and the environmental vibration. The average trapping time was measured as a function of the optical power (Figure 3e). The result shows that when the power was larger than  $3 \text{ mW}$ , the trapping time increased linearly with the power, because the optical force is proportional to the power [24].

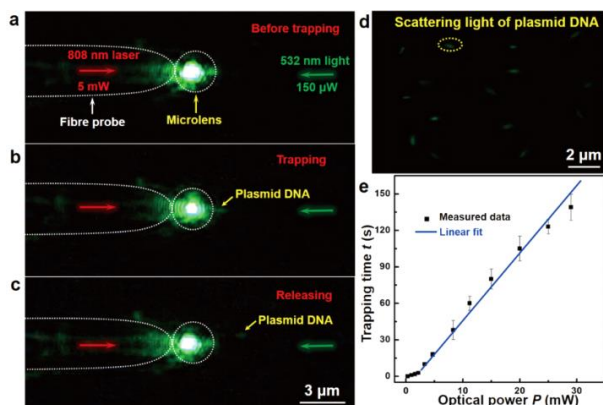


**Fig. 13.** Optical trapping of a single DNA molecule. (a)–(c) Dark-field images: (a) before trapping, (b) during trapping and (c) releasing a single DNA molecule. (d) Dark-field image of DNA molecules illuminated with 532-nm light. The yellow dotted ellipse denotes the scattered light from a single DNA molecule. (e) Trapping time  $t$  as a function of optical power  $P$  with a linear fitting for  $P \geq 3 \text{ mW}$  [24].

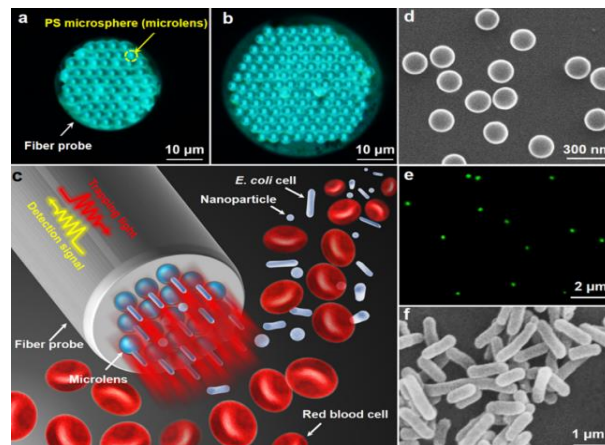


**Fig. 14.** Optical images of arrays of (a) 60 and (b) 130 microlenses. (c) Schematic showing selective manipulation and detection of multiple nanoparticles and subwavelength cells in a human blood solution using a parallel photonic nanojet array. (d) SEM image of nanoparticles with average diameter of  $190 \text{ nm}$ . (e) Optical image of nanoparticles in the solution when excited by a  $398 \text{ nm}$  laser beam. (f) SEM image of *E. coli* cells with average diameter of  $400 \text{ nm}$  and average length of  $2.6 \mu\text{m}$  [25].

In addition to trapping and manipulation of a single nano-objects, multiple nano-objects can be also simultaneously trapped with an OFP by using a parallel photonic nanojet array [25]. To generate the nanojet array, a two-dimensional array of microlenses was regularly assembled on the end face of a flat OFP via a photophoretic technique, which has been demonstrated as an efficient method to assemble two-dimensional crystals on a flat surface [86]. As results, Fig. 14a shows an optical image of 60 microlenses assembled on an OFP with a diameter of  $28 \mu\text{m}$ , and Fig. 14b depicts a large-scale microlens array formed by assembling 130 microlenses on an OFP with a diameter of  $45 \mu\text{m}$ . Fig. 14c schematically shows multiple objects, such as PS nanoparticles and sub-wavelength cells can be selectively trapped in a human blood solution by using the parallel photonic nanojet array. The device based on the OFP bound with a microlens array, making it highly autonomous and free of bulky optical system. The flexibility and miniaturization of this device allow it to operate in narrow spaces such as blood vessels or lab-on-a-chip microfluidics. To experimentally demonstrate the trapping and manipulation ability of the photonic nanojet array, fluorescent nanoparticles (Fig. 14d), with emission at  $518 \text{ nm}$  (Fig. 14e) were used as targets. As an example of a biological application of the device, *E. coli* cells with an average diameter of  $400 \text{ nm}$  (Fig. 14f) were also prepared for the experiments. A trapping laser beam with an optical power of  $60.2 \text{ mW}$  was directed into the OFP for trapping applications. This means that an average optical power of about  $1.0 \text{ mW}$  was released on a single microlens. When they were irradiated by the trapping laser beam, the fluorescent nanoparticles that were located near the tip of the OFP were trapped in the photonic nanojet array by the strong optical gradient force that is exerted on the nanoparticles. With controlled movement of the OFP in the suspension, more nanoparticles can be efficiently

trapped into the nanojet array. An optical microscope image shows that a single nanoparticle was trapped by each photonic nanojet (Fig. 15a). During the trapping experiment, no obvious heating effects, such as thermophoresis or fluidic convection, were observed, and so that the trapped nanoparticles can be maintained stably until the trapping light was switched off. In addition to the PS nanoparticles, the photonic nanojet array can also trap biological species with subwavelength sizes such as *E. coli* cells, as described in Fig. 15b. Interestingly, all the trapped cells tend to align their long axes along the optical axis because this orientation was the most stable state. To confirm the nano-objects were actually trapped by the optical forces, additional experiments were performed and demonstrated that the trapped nanoparticles and *E. coli* cells can be released by switching the trapping laser off. When the nanoparticles or cells were trapped by the photonic nanojets, their backscattering signals could be detected in real time with single-nanoparticle resolution (Fig. 15c). Several obvious abrupt increases in the signal are observed, which were induced by the scattering light of the trapped nano-objects. Fig. 15d shows histograms of the signal intensity fitted with Gaussian distributions. The center intensity and the FWHM of the distributions increased when more nano-objects was added to the photonic nanojet, which was resulted from the stronger light backscattering and the increased Brownian motion of the nano-objects. Because the backscattering signal is sensitive and specific to the trapped nano-objects, it can be used to identify different kinds of nano-objects. Besides, a contrast experiment was also performed by using the same OFP but without the microlenses. The experimental results shows that the backscattering signal of the nano-objects cannot be detected using the bare OFP alone, which confirms that the single-nanoparticle-resolution detection was benefited from the signal enhancement abilities of the photonic nanojets.

The OFP-microlens-supported photonic nanojet technique provides a near-field method for optical nanomanipulation of sub-100-nm nanoparticles and biomolecules. This technique requires no bulk high-NA objectives, nanofabrication processes and complex nanostructures that are fixed on a substrate. With advantages of high manipulation freedom, signal enhancement, real-time detection and low optical power consumption, the proposed method is expected to open exciting new opportunities for applications in a wide variety of scientific fields, ranging from nanostructure assembly to single-molecule analysis [24]. Furthermore, the parallel photonic nanojet array method makes use of the two-dimensional microlens array on a compact OFP, which is simple to fabricate and integrate. The strong confinement of the nanojet array provides large optical trapping force, which enables the stable trapping of nanoparticles and subwavelength cells at a relatively low optical power. Additionally, the nanojet arrays can be used to selectively trap one type of nanoparticles or cells in a mixture, such as human blood. Therefore, the

nanojet array is potentially a powerful tool for optical sorting and biosensing of pathogenic bacteria [25].

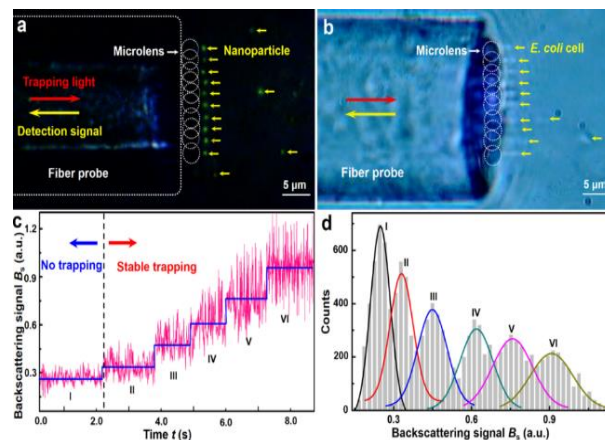


**Fig. 15.** Manipulation of multiple nanoparticles and *E. coli* cells. (a) Optical trapping of multiple 190-nm fluorescent PS nanoparticles using the photonic nanojet array. (b) Optical trapping of multiple *E. coli* cells using the photonic nanojet array. (c) Real-time detection of backscattering signal  $B_s$  during the trapping of multiple PS nanoparticles. Each of the steps (I–VI) in  $B_s$  indicates that a single nanoparticle trapping event has occurred. (d) Histogram showing  $B_s$  intensity distributions with Gaussian fittings [25].

## Conclusion and future perspectives

In this review, starting from the basic origin of the optical forces at the nanoscale, we have shown OFP-based optical trapping and manipulation of different nanomaterials, including carbon nanotubes, silver and semiconductor nanowires, upconversion fluorescence and polystyrene nanoparticles, and DNA molecules. These fibre-optic techniques possess many unique advantages. First, they can realize stable trapping and controllable manipulation of single or multiple nano-objects in a noninvasive and noncontact manner for various applications. Second, avoiding the use of bulky optical systems and complex nanostructures, OFPs are becoming flexible, miniaturized, simple and handy tools, which thus enhance the prospects of applications of these techniques in the biophotonics, nanophotonics, and biomedical fields. The OFP-based nanomanipulation provides new possibilities as well as new insights for applications in nanostructure assembly, high-resolution biosensing, single-cell analysis, and single-molecule studies.

With the recent progresses and advances, we anticipate the following research trends in fibre-optic nanomanipulation. First, most current nano-optical manipulations are performed in water, air, or other homogenous environments. When the medium is inhomogeneous, especially *in-vivo* systems, however, the nanomanipulation become a great challenge because the light scattering from biological tissues makes the optical forces much more complex. Therefore, considerable efforts might be focused on *in-vivo* manipulation of nano-objects, such as viruses, vesicles, proteins or nucleic acid molecules. The flexibility and miniaturization of the OFP may allow it to become a

promising candidate for *in-vivo* optical nanomanipulation. Second, stably trapping and spatially controlling sub-10-nm objects in an accurate resolution is a key issue to building new functional nano-devices. There is an attractive goal for optical fibre nanomanipulation to extend the limit into sub-10-nm range. Overall, the fibre-optic nano-trapping and manipulation with multifunctional ability and ultra-accurate resolution may find diverse promising applications in biology, physics and engineering.

#### Acknowledgements

This work was supported by the National Natural Science Foundation of China (No. 11774135).

#### Supporting information

Supporting informations are available from VBRI Press.

#### References

1. Ashkin, A.; *Phys. Rev. Lett.* **1970**, *24*, 156.
2. Grier, D. G.; *Nature* **2003**, *424*, 810.
3. Dholakia, K.; Reece, P.; Gu, M.; *Chem. Soc. Rev.* **2008**, *37*, 42.
4. Dholakia, K.; Reece, P.; *Nano Today*, **2006**, *1*, 18.
5. Neuman, K. C.; Block, S. M.; *Rev. Sci. Instrum.* **2004**, *75*, 2787.
6. Bustamante, C.; Bryant, Z.; Smith, S. B.; *Nature* **2003**, *421*, 423.
7. Ashkin, A.; *Proc. Nat. Acad. Sci. USA* **1997**, *94*, 4853.
8. Ashkin, A.; Dziedzic, J. M.; Yamane, T.; *Nature* **1987**, *330*, 769.
9. Daly, M.; Sergides, M.; Nic, Chormaic, S.; *Laser Photonics Rev.* **2015**, *9*, 309.
10. Maragò, O. M.; Jones, P. H.; Gucciardi, P. G.; Volpe, G.; Ferrari, A. C.; *Nat. Nanotechnol.* **2013**, *8*, 807.
11. Erickson, D.; Serey, X.; Chen, Y. F.; Mandal, S.; *Lab Chip* **2011**, *11*, 995.
12. Quidant, R.; Girard, C.; *Laser Photonics Rev.* **2008**, *2*, 47.
13. Jesacher, A.; Fürhapter, S.; Bernet, S.; Ritsch-Marte, M.; *Opt. Express* **2004**, *12*, 4129.
14. Berthelot, J.; Acimović, S. S.; Juan, M. L.; Kreuzer, M. P.; Renger, J.; *et al. Nature Nanotech.* **2014**, *9*, 295.
15. Yang, A. H.; Moore, S. D.; Schmidt, B. S.; Klug, M.; Lipson, M.; *et al. Nature* **2009**, *457*, 71.
16. Mandal, S.; Serey, X.; Erickson, D.; *Nano Lett.* **2010**, *10*, 99.
17. Chen, Y. F.; Serey, X.; Sarkar, R.; Chen, P.; Erickson, D.; *Nano Lett.* **2012**, *12*, 1633.
18. Serey, X.; Mandal, S.; Chen, Y. F.; Erickson, D.; *Phys. Rev. Lett.* **2012**, *108*, 048102.
19. Xin, H.; Xu, R.; Li, B.; *Sci. Rep.* **2012**, *2*, 818.
20. Xu, X.; Cheng, C.; Xin, H.; Lei, H.; Li, B.; *Sci. Rep.* **2014**, *4*, 3989.
21. Xu, X.; Cheng, C.; Zhang, Y.; Lei, H.; Li, B.; *Sci. Rep.* **2016**, *6*, 29449.
22. Berthelot, J.; Acimović, S.; Juan, M.; Kreuzer, M.; Renger, J.; Quidant, R.; *Nature Nanotech.* **2014**, *9*, 295.
23. Xin, H.; Li, B.; *Light: Sci. Appl.* **2014**, *3*, e205.
24. Li, Y.-C.; Xin, H.-B.; Lei, H.-X.; Liu, L.-L.; Li, Y.-Z.; Zhang, Y.; Li, B.-J.; *Light: Sci. Appl.* **2016**, *5*, e16176.
25. Li, Y.; Xin, H.; Liu, X.; Zhang, Y.; Lei, H.; Li, B.; *ACS Nano* **2016**, *10*, 5800.
26. Xin, H.; Li, Y.; Xu, D.; Zhang, Y.; Chen, C. H.; Li, B.; *Small* **2017**, *13*, 1603418.
27. Li, Y.; Liu, X.; Yang, X.; Lei, H.; Zhang, Y.; Li, B.; *ACS nano* **2017**, DOI: [10.1021/acsnano.7b04420](https://doi.org/10.1021/acsnano.7b04420).
28. Cheng, C.; Xu, X.; Lei, H.; Li, B.; *RSC Adv.* **2014**, *4*, 21593.
29. Liu, Z.; Guo, C.; Yang, J.; Yuan, L.; *Opt. Express* **2006**, *14*, 12510.
30. Liberale, C.; Minzioni, P.; Bragheri, F.; De Angelis, F.; Di Fabrizio, E.; Cristiani, I.; *Nature Photon.* **2007**, *1*, 723.
31. Daly, M.; Truong, V. G.; Phelan, C.; Deasy, K.; Chormaic, S. N.; *New J. Phys.* **2014**, *16*, 053052.
32. Zhang, Y.; Li, B.; *Laser Photonics Rev.* **2013**, *7*, 289.
33. Xin, H.; Li, Y.; Liu, X.; Li, B.; *Nano Lett.* **2013**, *13*, 3408.
34. Xin, H.; Xu, R.; Li, B.; *Laser Photonics Rev.* **2013**, *7*, 801.
35. Li, Y.; Xin, H.; Cheng, C.; Zhang, Y.; Li, B.; *Nanophotonics* **2015**, *4*, 353.
36. Li, Y.; Xin, H.; Liu, X.; Li, B.; *Sci. Rep.* **2015**, *5*, 10925.
37. Xin, H.; Li, Y.; Li, B.; *Adv. Funct. Mater.* **2015**, *25*, 2816.
38. Xin, H.; Li, Y.; Li, B.; *Laser Photonics Rev.* **2015**, *9*, 554.
39. Gordon, J. P.; *Phys. Rev. A.* **1973**, *8*, 14.
40. Albaladejo, S.; Marqués, M. I.; Laroche, M.; Sáenz, J. J.; *Phys. Rev. Lett.* **2009**, *102*, 113602.
41. Draine, B. T.; *Astrophys. J.* **1988**, *333*, 848.
42. Albaladejo, S.; Marqués, M. I.; Laroche, M.; Sáenz, J. J.; *Phys. Rev. Lett.* **2009**, *102*, 113602.
43. Mishchenko, M. I.; *J. Quant. Spectrosc. Radiat. Transfer* **2001**, *70*, 811.
44. Saija, R.; Iatí, M. A.; Giusto, A.; Denti, P.; Borghese, F.; *J. Quant. Spectrosc. Radiat. Transfer* **2005**, *94*, 163.
45. Borghese, F.; Denti, P.; Saija, R.; Iatí, M. A.; *Opt. Express* **2006**, *14*, 9508.
46. Hu, L.; Hecht, D. S.; Gruner, G.; *Chem. Rev.* **2010**, *110*, 5790.
47. De Volder, M. F.; Tawfick, S. H.; Baughman, R. H.; Hart, A. J.; *Science* **2013**, *339*, 535.
48. Kosynkin, D. V.; Higginbotham, A. L.; Sinitiskii, A.; Lomeda, J. R.; Dimiev, A.; Price, B. K.; Tour, J. M.; *Nature* **2009**, *458*, 872.
49. Jiao, L.; Xian, X.; Wu, Z.; Zhang, J.; Liu, Z.; *Nano Lett.* **2009**, *9*, 205.
50. Liu, H.; Takagi, D.; Chiashi, S.; Homma, Y.; *ACS Nano* **2010**, *4*, 933.
51. Wang, Y.; Maspoch, D.; Zou, S.; Schatz, G. C.; Smalley, R. E. *et al. Proc. Natl. Acad. Sci. USA* **2006**, *103*, 2026.
52. Kang, P.; Serey, X.; Chen, Y.-F.; Erickson, D.; *Nano Lett.* **2012**, *12*, 6400.
53. Zhang, J.; Kim, H. I.; Oh, C. H.; Sun, X.; Lee, H.; *Appl. Phys. Lett.* **2006**, *88*, 053123.
54. Rodgers, T.; Shoji, S.; Sekkat, Z.; Kawata, S.; *Phys. Rev. Lett.* **2008**, *101*, 127402.
55. Dittbacher, H. *et al. Phys. Rev. Lett.* **2005**, *95*, 257403.
56. Halas, N. J.; Lal, S.; Chang, W.; Link, S.; Nordlander, P.; *Chem. Rev.* **2011**, *111*, 3913.
57. Yan, R.; Gargas, D.; Yang, P.; *Nature Photon.* **2008**, *3*, 569.
58. Fang, Y. *et al. Nano Lett.* **2010**, *10*, 1950.
59. Pauzauskie, P. J. *et al. Nature Mater.* **2006**, *5*, 97.
60. Xu, S. *et al. Adv. Mater.* **2010**, *22*, 4749.
61. Chen, C. *et al. ACS Nano* **2011**, *5*, 6707.
62. Devan, R. S.; Patil, R. A.; Lin, J. H.; Ma, Y. R.; *Adv. Funct. Mater.* **2012**, *22*, 3326.
63. Wang, Z. L. *Mater. Sci. Eng., R* **2009**, *64*, 33.
64. van der Horst, A. *Opt. Express* **2007**, *15*, 11629.
65. Li, X.; Zhang, F.; Zhao, D.; *Chem. Soc. Rev.* **2015**, *44*, 1346.
66. Zhou, B.; Shi, B.; Jin, D.; Liu, X. *Nat. Nanotechnol.* **2015**, *10*, 924.
67. Zhao, J. *et al. Nat. Nanotechnol.* **2013**, *8*, 729.
68. Wang, F.; Liu, X. *Chem. Soc. Rev.* **2009**, *38*, 976.
69. Ong, L. C.; Ang, L. Y.; Alonso, S.; Zhang, Y. *Biomaterials* **2014**, *35*, 2987.
70. Pan, W.; Zhao, J.; Chen, Q. *J. Agric. Food Chem.* **2015**, *63*, 8068.
71. Boyer, J. C.; Van Veggel, F. C. *Nanoscale* **2010**, *2*, 1417.
72. Mannoor, M. S. *et al. Nat. Commun.* **2012**, *3*, 763.
73. Haandbæk, N.; Bürgel, S. C.; Heer, F.; Hierlemann, A. *Lab Chip* **2014**, *14*, 3313.
74. Kim, M. S.; Scharf, T.; Mühlig, S.; Rockstuhl, C.; Herzig, H. P.; *Opt. Express* **2011**, *19*, 10206.
75. Yang, H.; Cornaglia, M.; Gijs, M. A.; *Nano Lett.* **2015**, *15*, 1730.
76. Chen, Z.; Taflove, A.; Backman, V.; *Opt. Express* **2004**, *12*, 1214.
77. Wang, Z. *et al. Nature Commun.* **2011**, *2*, 218.
78. Yan, Y. *et al. ACS Nano* **2014**, *8*, 1809.
79. Mcleod, E.; Arnold, C. B.; *Nature Nanotech.* **2008**, *3*, 413.
80. Kasim, J. *et al. Opt. Express* **2008**, *16*, 7976.
81. Alessandri, I.; Bontempi, N.; Depero, L. E.; *RSC Adv.* **2014**, *4*, 38152.
82. Berg-Sørensen, K.; Flyvbjerg, H. *Rev. Sci. Instrum.* **2004**, *75*, 594.
83. Tolić-Nørrelykke, S. F.; Schäffer, E.; Howard, J.; Pavone, F. S.; Jülicher, F.; *Rev. Sci. Instrum.* **2006**, *77*, 103101.
84. Juan, M. L.; Gordon, R.; Pang, Y.; Eftekhari, F.; Quidant, R.; *Nature Phys.* **2009**, *5*, 915.
85. Grigorenko, A. N.; Roberts, N. W.; Dickinson, M. R.; Zhang, Y.; *Nature Photon.* **2008**, *2*, 365.
86. Lei, H.; Zhang, Y.; Xu, C.; Li, B.; *J. Opt.* **2012**, *14*, 035603.